

# Energy & Environmental Science

Accepted Manuscript



This is an *Accepted Manuscript*, which has been through the Royal Society of Chemistry peer review process and has been accepted for publication.

*Accepted Manuscripts* are published online shortly after acceptance, before technical editing, formatting and proof reading. Using this free service, authors can make their results available to the community, in citable form, before we publish the edited article. We will replace this *Accepted Manuscript* with the edited and formatted *Advance Article* as soon as it is available.

You can find more information about *Accepted Manuscripts* in the [Information for Authors](#).

Please note that technical editing may introduce minor changes to the text and/or graphics, which may alter content. The journal's standard [Terms & Conditions](#) and the [Ethical guidelines](#) still apply. In no event shall the Royal Society of Chemistry be held responsible for any errors or omissions in this *Accepted Manuscript* or any consequences arising from the use of any information it contains.

# Functional Links Between Pt Single Crystal Morphology and Nanoparticles with Different Size and Shape: the Oxygen Reduction Reaction Case

Dongguo Li,<sup>†,‡</sup> Chao Wang,<sup>†</sup> Dusan S. Strmcnik,<sup>†</sup> Dusan V. Tripkovic,<sup>†</sup> Xiaolian Sun,<sup>‡</sup> Yijin Kang,<sup>†</sup> Miaofang Chi,<sup>¶</sup> Joshua D. Snyder,<sup>†</sup> Dennis van der Vliet,<sup>†</sup> Yifen Tsai,<sup>§</sup> Vojislav R. Stamenkovic,<sup>†</sup> Shouheng Sun<sup>‡</sup> and Nenad M. Markovic<sup>†\*</sup>

<sup>†</sup> Materials Science Division, Argonne National Laboratory, Argonne, IL 60439, USA

<sup>‡</sup> Department of Chemistry, Brown University, Providence, RI 02912, USA

<sup>¶</sup> Division of Material Science and Technology, Oak Ridge National Laboratory, Oak Ridge, TN 37831, USA

<sup>§</sup> Chemical Science and Engineering Division, Argonne National Laboratory, Argonne, IL 60439, USA

## ABSTRACT

Design of active and stable Pt-based nanoscale electrocatalysts for the oxygen reduction reaction (ORR) will be the key to improving the efficiency of fuel cells that are needed to deliver reliable, affordable and environmentally friendly energy. Here, by exploring the ORR on Pt single crystals, cubo-octahedral (polyhedral) Pt NPs with different sizes (ranging from 2 to 7 nm), and 7-8 nm Pt NPs with different shapes (cubo-octahedral vs. cube vs. octahedral), we presented surface science approach capable of rationalizing, and ultimately understanding, fundamental relationships between stability of Pt NPs and activity of the ORR in acidic media. By exploring the potential induced dissolution/re-deposition of Pt between 0.05 and 1.3 V, we found that concomitant variations in morphology of Pt(111) and Pt(100) lead to narrowing differences in activity between Pt single crystal surfaces. We also found that regardless of an initial size or shape, NPs are metastable and easily evolve to thermodynamically equilibrated shape and size with very similar activity for the ORR. We concluded that while initially clearly observed, the particle size and shape effects diminish as the particles age to the point that it may appear that the ORR depends neither on the particle size nor particle shape.

## Introduction

The last two decades have witnessed remarkable progress in our ability to chemically synthesize metal nanoparticles (NPs) ranging in size from 1 to 10 nm with unique electrocatalytic properties.<sup>1-4</sup> Because the electronic properties of metal NPs in this size range are not unique,<sup>5</sup> (electro)catalyst research with such materials has focused on the variations in the reaction rate or selectivity with characteristic dimensions of metallic catalysts. While Boronin and co-workers<sup>6</sup> pioneered this approach to understand the “crystalline size effect” in heterogeneous catalysis, Kinoshita<sup>7</sup> and others<sup>8,9</sup> used this tactic to understand the “particle size effect” in electrocatalysis. There is no simple ideal structure that will model all the aspects of NP catalysts, particularly in the configuration that are used in electrolytic cells. However, if one considers the equilibrium shape of a face-centered cubic (*fcc*) metal NP such as a cubo-octahedron, consisting of (111) and (100) facets bounded by edge atom rows that are like the top-most rows in the (110) surface, single-crystal surfaces may serve as a reasonable model for

assessing the particle size and shape effects for reactions that present a certain structure sensitivity. Structure sensitivity refers to the dependence of reaction rate on the geometry of surface atoms<sup>10,11</sup>. One class of electrochemical reaction exhibiting strong structure sensitivity is the oxygen reduction reaction (ORR), the cathodic half-cell reaction in fuel cells.<sup>12,13,14</sup>

In contrast to structure sensitivity, the Pt particle size effect on the ORR is still controversial. While some authors claim that there is a difference in activity between different particle sizes,<sup>15–19</sup> there are also reports claiming that little or no particle size effects exist for the ORR within specific size range.<sup>20–22</sup> Even less is known about a functional link between surface structure sensitivity and the shape of Pt NPs,<sup>18,23,24</sup>. In general, longstanding difficulty in resolving the particle size and shape effects can be attributed to a lack of methods suitable for syntheses of impurity-free Pt NPs that are uniform in size, equally dispersed on a conductive support and can be characterized at atomic and molecular levels. This situation is in sharp contrast to that for Pt single crystals, for which the developments of surface preparation and characterization techniques have been well established over the last three decades.<sup>25</sup> Additionally, unlike Pt(hkl) single crystals where adsorption and catalytic properties can be obtained in the very first electrode potential sweep,<sup>26</sup> Pt NPs are often deactivated (poisoned) by the residual surfactants from the colloidal Pt NPs synthesis. Surfactants are commonly removed by prolonged potential cycling in the potential region where an irreversible Pt-oxide is formed, leading inevitably to continual change in particle size and shape;<sup>27–30</sup> an issue which has often been overlooked in electrocatalysis on metal NPs. Based on these and many other challenges,<sup>16,31</sup> one may anticipate that depending on the experimental conditions and/or the physical properties of NPs, one may or may not find any correlation between the particle size and/or shape and activity for electrochemical reactions. However, finally resolving this controversial subject would be of fundamental and technological importance.

Here, we demonstrate that it is possible to develop a distinctive and systematic experimental strategy that reveals the inherently close ties between the structure sensitivity and the particle size/shape effects for the ORR ( $\text{O}_2 + 4\text{H}^+ + 4\text{e}^- = 2\text{H}_2\text{O}$ ) on Pt single crystals and Pt NPs in acidic environments. First, we establish symbiotic relationship between the oxide-induced morphological changes of Pt(111) and Pt(100) and the kinetics of the ORR. Then, we use these results as a foundation for developing a new experimental protocol for resolving the particle size and shape effects. By studying the ORR on four types of cubo-octahedral NPs with sizes ranging from 2.8–7.2 nm we establish that if the NPs are well dispersed and uniform in size then the ORR activity indeed depends on the size of Pt NPs. On the other hand, by studying the ORR on cubo-octahedral, cubic and octahedral NPs we found that the particle shape effect is much smaller, especially after moderate potential cycling. We propose that this is because under ORR relevant conditions the particle size and shape effects are constantly evolving due to the potential-induced transformations of both the smaller particles to larger particles as well as cubo-octahedral, cubic and octahedral NPs to round-like shaped NPs. Thus, while initially clearly observed, the particle size and shape effects diminish as the particles age to the point that it may appear that the ORR depends neither on the particle size nor particle shape.

### **Structure-function relationships: the ORR on Pt single crystal surfaces**

Although it is well established that the ORR is structure sensitive reaction,<sup>12,14,32–35</sup> no attempts have been made to resolve the fundamental link between the activity and potential-dependent changes in morphology of Pt single crystal surfaces (stability of surface atoms),

especially after introduction of an irreversible oxide and its subsequent reduction. As we present further below, establishing such relations is one key in undertaking the particle size and particle shape effects in electrocatalysis.

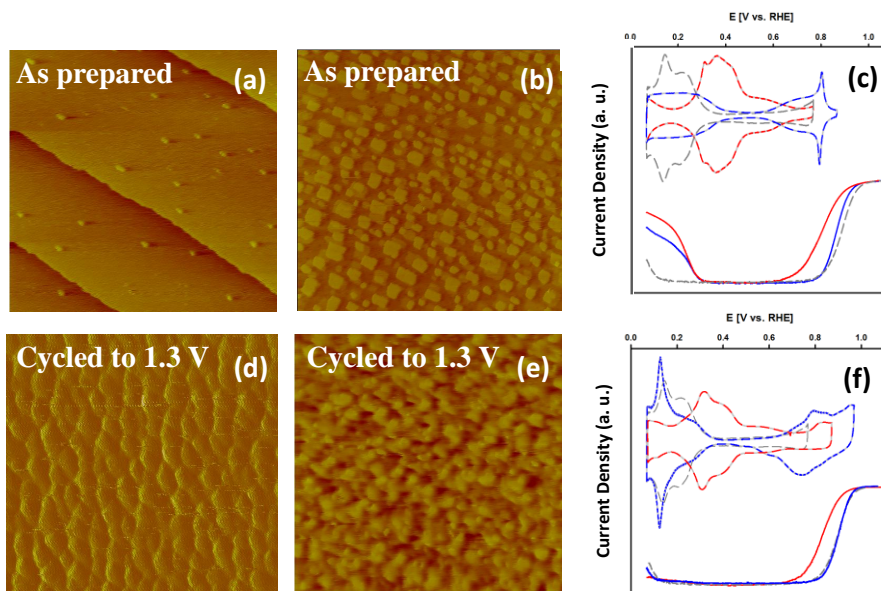


**Figure 1.** Ex-situ STM images of as prepared (a) Pt(111) and (b) Pt(100). (c) Cyclic voltammograms and corresponding ORR polarization curves of as prepared Pt(100) (red line), Pt(111) (grey line) and Pt(111) (blue line). Ex-situ STM images of (d) Pt(111) and (e) Pt(100) after cycled to 1.3 V. (f) Cyclic voltammograms and ORR polarization curves of Pt(100) (red line) and Pt(111) (blue line) after cycled to 1.3 V compared to as prepared Pt(111) (grey line). All the CV and ORR were measured in 0.1 M HClO<sub>4</sub>.

We start with the analysis of the ex-situ scanning tunneling microscopy (STM) images that, as in the past,<sup>36–39</sup> we use to characterize the potential-dependent variations in morphology of Pt single crystal surfaces. The basic experimental protocol introduced here is to acquire STM images first and then to analyze how the morphological changes induced by irreversible oxide formation affect the voltammetric features corresponding to the underpotentially deposited hydrogen ( $H_{\text{upd}}$ ) and oxygenated species ( $\text{OH}_{\text{ad}}$ )<sup>38</sup> and ultimately the ORR. For example, while an STM image of the as-prepared Pt(111) electrode reveals that at 0.05 V the surface is composed of a flat terrace which is covered by few steps and Pt ad-islands with monatomic height (Figure 1a), ad-islands with square shapes and monoatomic height are clearly evident on the as-prepared Pt(100) electrode (Figure 1b). The presence of such islands on Pt(100) is due to “lifting” of a (100)-hex phase and the formation of a (100)-(1x1) surface with “well-ordered” defects.<sup>40</sup> Importantly, the as-prepared surface morphology of these single-crystals remain unchanged after 100 cycles between 0.05 V and 0.85 V, confirming that the reversible adsorption of  $\text{OH}_{\text{ad}}$  does not result in Pt dissolution and thus surface roughening. As a consequence, and in agreement with previous literature, after potential cycling up to 0.85V a stable CVs are observed for Pt(100) and Pt(111). Figure 1c shows that while on Pt(100) adsorption of hydroxyl species overlaps with the adsorption of hydrogen below 0.45 V, the adsorption of  $\text{OH}_{\text{ad}}$  above 0.6 V on Pt (111) (usually termed as the “butterfly peak”) is clearly separated from the  $H_{\text{upd}}$  potential region.<sup>26</sup> By comparing the CVs with their corresponding STM images it is obvious that, in fact, there are no truly defect-free single-crystals and, CVs are insensitive to the dispersed atomic scale

morphology defects inherently present on as-prepared single-crystal surfaces (for more details see also reference<sup>38,41</sup>). Nevertheless, Figure 1c also show that the ORR is indeed structure sensitive reaction, under our experimental conditions Pt(111) being more active than Pt(100); this is because the surface coverage by spectator adsorbates such as  $\text{OH}_{\text{ad}}$  is lower on the former surface.<sup>12</sup>

The first visible effects of the oxide-induced dissolution/re-deposition of Pt and corresponding change in surface morphology, adsorption of  $\text{H}_{\text{upd}}$  and  $\text{OH}_{\text{ad}}$ , as well as the ORR are observed for a potential cycling above 0.95 V. For our purposes here, however, to track morphological changes on a reasonable time scale we have used an accelerated protocol with an upper potential limit of 1.3 V. As summarized in Figure 1, after the potential cycling to 1.3 V, visible “ordered” disordering of Pt(111) (Figure 1d) and Pt(100) (Figure 1e) is accompanied by the appearance of new  $\text{H}_{\text{upd}}$  peaks, and disappearance of the “butterfly feature” (Figure 1f). Based on CVs acquired on stepped single crystal surfaces<sup>34,42,43</sup>, a sharp reversible  $\text{H}_{\text{upd}}$  peak observed at 0.175 V on a “rough” Pt(111) electrode can be assigned to hydrogen adsorption along (111)-(111) step-edges. On the other hand,  $\text{H}_{\text{upd}}$  peak recorded at 0.375 V on a “rough” Pt(100) electrode corresponds to the hydrogen adsorption/desorption along (111)-(100) step-terrace like structures. Most importantly, Figure 1d-f reveal that the activity of ORR is improving by systematic roughening of Pt(111) and Pt(100), to the point that the activity of both surfaces is approaching the activity of Pt(110) (see Figure 1f). On the basis of these results, we conclude that the oxide-induced changes in surface morphology of Pt(111) and Pt(100) leads to formation of characteristic step-edge sites that narrow the differences in activity between Pt single crystal surfaces. In the following, the potential-dependent changes in surface morphology, adsorption, and reactivity properties observed on Pt(100) and Pt(111) will be used as a foundation for discussing the particle size and shape effects in the ORR.

### Particle size effect: the ORR on cubo-octahedral NPs

Recall that the longstanding difficulty in resolving the particle size effects has been attributed to a lack of methods suitable for syntheses of impurity-free Pt NPs that are uniform in size and equally dispersed on a conductive support, as well as to a lack of experimental protocol that will allow monitoring variation in activity and stability under the same experiment conditions.<sup>7,15-17,19,44-46</sup> Here, by implementing the experimental protocol developed for finding relationships between activity and stability of Pt single crystals (Figure 1), we demonstrate that it would be possible to acquire related potential-dependent variations in the size of NPs and their activity and stability. For example, TEM images at low magnification show that as-synthesized NPs with diameters of  $2.8 \pm 0.4$  nm (Figure 2a),  $4.1 \pm 0.5$  nm (Figure 2b),  $5.1 \pm 0.4$  nm (Figure 2c) and  $7.2 \pm 0.6$  nm (Figure 2d) have uniform size (for histograms of particle size distribution see Fig. S2). Significantly, supported NPs on high surface area carbon remain well-dispersed, preserving uniform sizes even after surfactant removal (for details see the Experimental Methods). For corresponding CVs, summarized in Figure 2e, two distinguished features are noteworthy. First, independent of the particle size, two clearly resolved reversible  $\text{H}_{\text{upd}}$  peaks (positioned at 0.1 V and 0.275 V) can be assigned to hydrogen adsorption along (111)-(111) and (111)-(100) step-edges (assignment based on results for Pt single crystal surfaces in Figure 1c). Second, the position of the oxide formation/reduction peaks shifts systematically towards more positive potentials with increasing particle size, confirming that oxophilicity of Pt NPs increases from 7.2 nm to 2.8 nm.<sup>17,33</sup>

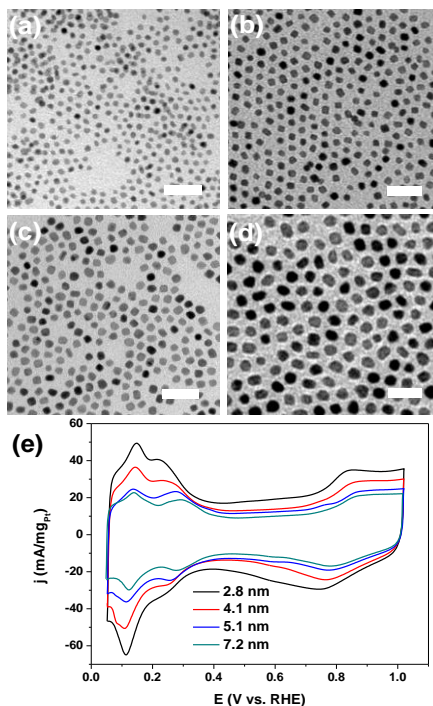


**Figure 2.** TEM images for the as-synthesized (a)  $2.8 \pm 0.4$  nm, (b)  $4.1 \pm 0.5$  nm, (c)  $5.1 \pm 0.4$  nm, (d)  $7.2 \pm 0.6$  nm Pt nanoparticles. Scale bar equals 20 nm. (e) Corresponding cyclic voltammograms recorded at 50mV/s scan rate in Ar purged 0.1 M perchloric acid.

In agreement with observations made with low index Pt single crystals, prolonged cycling over potential regions between 0.05 and 0.8 V had no substantial effect on the shape of CVs, indicating that during our experiment the NPs appear to be rather stable. The first visible effects of the oxide-induced dissolution/re-deposition of Pt are observed for a potential cycling above 0.9 V (Fig. S3). Provided that morphological changes observed after potential cycling up to 1.0 V were rather slow, to monitor the potential-induced changes in morphology of NPs on a reasonable time scale we have also used an accelerated catalyst degradation protocol with an upper potential limit of 1.1 V (see Figure 3a-3f). For example, the resulting TEM images of 2.8 nm particles show that the extensive cycling up to 1.1 V causes a significant increase in the NPs average size (Figures 3a and 3b) -- from 2.8 nm to 7.3 nm with a concomitant increase in the polydispersity and a significant fraction of particles with diameters greater than 10 nm. This is indicative of an extensive dissolution of small nanoparticles followed by re-deposition of Pt resulting in the growth of larger particles. Not surprisingly, the electrochemically active surface area (ECSA) under the  $H_{\text{upd}}$  and  $OH_{\text{ad}}$  peaks decreases significantly after the potential cycling, as shown in Figure 3c. In sharp contrast, Figures 3d and 3e reveal that under the same experimental conditions, 7.2 nm NPs are rather stable, which is confirmed by negligible changes in the CV after extended potential cycling (Fig. 3f). As anticipated, Figure 3g shows that while the ECSA for small NPs (e.g., for 2.8 and 4.1 nm NPs) decreases dramatically even after moderate potential cycling, the ECSA changes observed for larger particles (5.1 and 7.2 nm) are rather modest, confirming that the latter are much more stable.

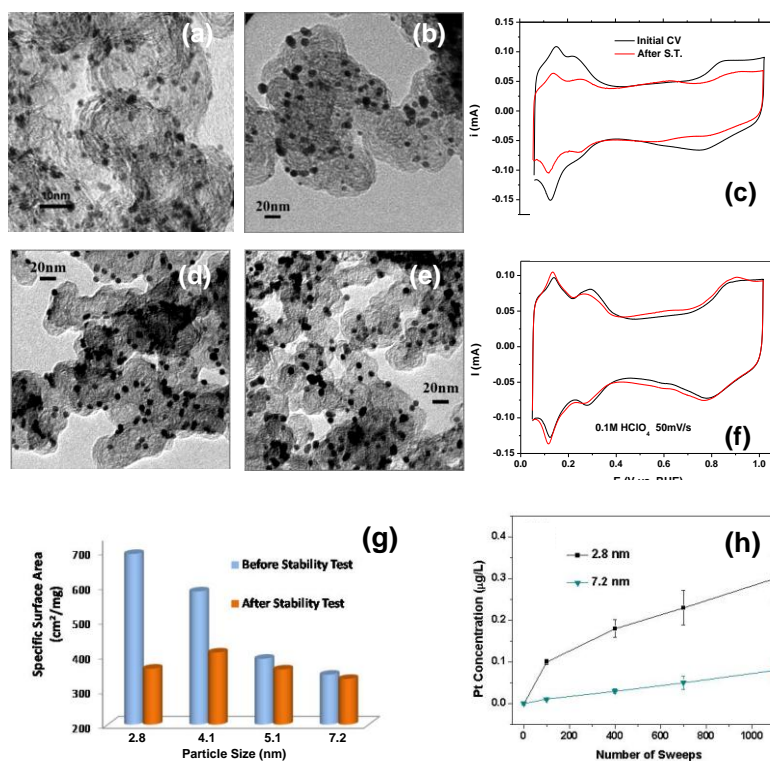


**Figure 3.** TEM images for the 2.8 nm Pt NPs on carbon support (a) before, (b) after stability test. (c) Cyclic voltammograms of 2.8 nm Pt/C NPs before (black curve) and after (red curve) stability test. TEM images of 7.2 nm Pt NPs on carbon support (d) before, (e) after stability test. (f) Cyclic voltammograms of 7.2 nm Pt/C NPs before (black curve) and after (red curve) stability test. (g) Summarized specific surface area of different sized NPs before (blue bar) and after (red bar) stability test. (h) Inductively coupled plasma mass spectrometry (ICPMS) method is used to assess Pt concentration in the electrolyte during potential cycling to 1.1 V for 2.8 nm (black line) and 7.2 nm particles (cyan line).

Stability of Pt NPs, measured as the amount of dissolved Pt cations in the electrolyte, was further examined by utilizing inductively coupled plasma mass spectrometry (ICPMS) method. Figure 3h shows that dissolved Pt content is four times higher for the 2.8 nm than for the 7.2 nm NPs, implying that small nanoparticles are indeed less stable than the larger NPs. As a consequence, the corresponding change of ECSA is much more pronounced for the 2.8 nm than for the 7.2 nm NPs (See Fig. S4). Given that the density of low-coordinated Pt atoms affects the stability trends,<sup>47,48</sup> results in Figure 3 suggest that the density of low coordinated atoms plays a significant role in the relationships between stability (dissolution of Pt) and changes in morphology. In contrast to Pt single crystals, however, for Pt NPs it is impossible to find a true correlation between the morphology of surface atoms and the corresponding stability since in contrast to STM, TEM is not capable of providing information on the structure of surface atoms. However, on the basis of results for Pt(111) and Pt(100) it is reasonable to expect that low coordinated Pt atoms along the step-edges are much less stable than more coordinated atoms that are part of (111) and (100) terraces.

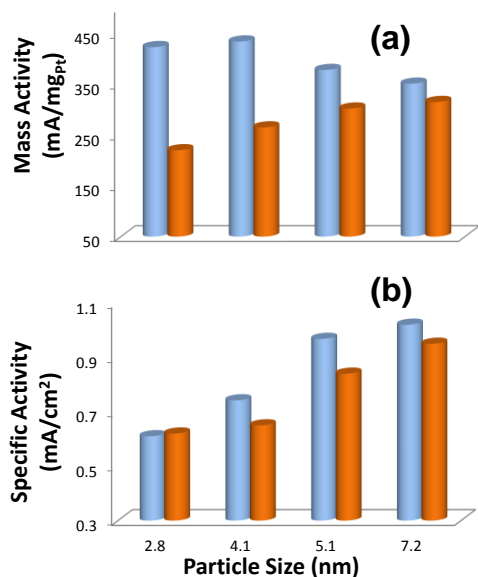


**Figure 4.** Effects of particle size on: (a) mass activity and (b) specific activity of ORR at 0.9 V before (blue bar) and after (red bar) stability test.

Furthermore, the average potential induced morphological changes of a carbon supported NP sample are not only linked to the finite size of the NPs but may also be tied to the particle size uniformity as well as stability of a carbon support (not discussed in this paper). In order to probe how the size distribution may affect the average morphological stability of supported NPs, we mixed 2.8 nm and 7.2 nm Pt/C catalyst suspensions with approximately 1:3 mass ratios. From Figure S5, TEM and electrochemical analyses of NPs unambiguously show that the variation in size of larger particles is substantial. This is an important observation considering that commercially available Pt catalysts (usually prepared by the impregnation method) are not as uniform in size as NPs produced by colloidal method used in this work. Therefore, any particle size effects observed on catalysts of this nature are not reliable as the system is not sufficiently well defined. We also find that the rate of catalyst degradation in terms of specific surface area and mass activity loss is accelerated for non-uniform size distributions. Not surprisingly, the overall stability performance of this mixture, with an average particle size of 5 nm, is found to be worse than that for the monodisperse 5 nm catalyst. As a result, it is obvious that having uniform particle size is also instrumental in monitoring the durability and activity of supported NP catalysts and thus establishing the particle size effect for the ORR.

The potential-induced variations in the mass and specific activity of the ORR are presented in Figure 4 where three key features are noteworthy (i) at the same overpotentials, specific activity increases by increasing the particle size, with the same trend in activity observed before and after potential cycling to 1.1 V; (ii) while mass activity before cycling above 1.0 V is increasing from larger (7.2nm) to a smaller NPs (4.1 nm), an inverse trend is observed after cycling at high anodic potentials: and (iii) large variations in activity are observed between 2.8 nm and 5.1 nm particles, and upon potential cycling the smaller particles suffer greater loss in mass activity (note that the particle size for an optimal initial mass activity is ~4 nm in diameter). In addition,

based on the knowledge from single crystals, it is reasonable to suggest that the observed particle size effect is governed by the correlation between particle size and surface coverage of  $\text{OH}_{\text{ad}}$ , which decreases with an increase in the “size” of ordered low index facets and a decrease in the defect/low coordinated site density (see also Figure 2e and 3). Thus, in harmony with structure sensitivity it is reasonable to propose that at the same overpotentials an increase in specific activity by increasing the NPs size can be attributed to an increase in availability of bare Pt sites required for adsorption of  $\text{O}_2$  and the formation of reactive intermediates. Although there is no one to one correspondence between the potential-dependent variations in adsorption properties of single crystals and high surface area materials, for establishing the experimental protocol and understanding behavioral differences between various NPs, it is crucial to understand the evolution of well-defined interfaces under the same experimental conditions and operational protocols. As summarized further below the same applies to the particle shape effects.

### **Particle shape effect: the ORR on nano-cubes and nano-octahedrons**

The particle shape effect on the ORR is even less certain than the particle size effect because the preparation of catalysts with dispersed metal particles of well defined shapes is not straightforward, but has been helped recently by development of novel synthetic techniques based on the solvothermal colloidal method.<sup>1,3,4,49</sup> To overcome the particle size effect discussed above, we synthesized 7-8 nm Pt NPs with the cubic and octahedral shapes as we found previously for cubo-octahedral shape that close to 7 nm Pt NPs tended to be more stable than the smaller diameter NPs. TEM images of NPs with the cubic and octahedral shapes are summarized in Supplementary Section Figure S6. High-resolution TEM (HRTEM) and scanning transmission electron microscope (STEM) images for octahedral and cubic NPs are depicted in Figures 5. Analysis of TEM images reveals that the NPs with cubic ( $7.3 \pm 0.6$  nm in edge length, Fig. S6a) and octahedron shapes ( $8.6 \pm 0.8$  nm in edge length, Fig. S6c) have similar size range when compared to the 7 nm cubo-octahedral NPs (Fig. 2d). Therefore we are not expecting to have a significant impact from the particle size effect. It is interesting to note that the shape of the as-synthesized cubic NPs supported on carbon, Figure 5a, bears a striking resemblance to the square-shaped ad-islands observed on the as-prepared Pt(100) in Figure 1b. This interim similarity in the particle shapes, however, has a tendency to mask the inherent differences in the density and nature of surface defects present on NPs and single crystal surfaces. For example, by comparing CVs of Pt single crystals with cubic NPs, a sequence of three reversible  $\text{H}_{\text{upd}}$  peaks are found on NPs; two sharp peaks centered at 0.15 and 0.275 V and a broad peak between 0.3 and 0.4 V. Based on the position of the  $\text{H}_{\text{upd}}$  peaks on Pt(110) and Pt(100) in Figure 5c, the cubic NPs dispersed on a carbon support contain some sites with the (100) geometry (broad peak between 0.3 to 0.4 V) and many more defects with both (111)-(100) (sharp peak centered at 0.275 V) and (111)-(111) (a peak at 0.15 V) symmetry.<sup>25</sup> Therefore, it is clear from the CV that the cubic NPs are dominated with many defects which are not visible in the TEM image.

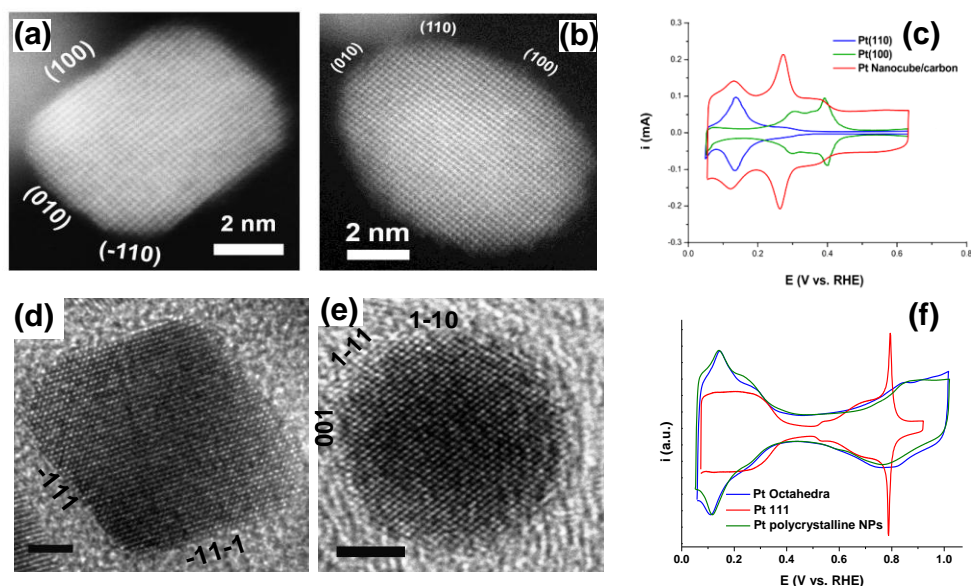


**Figure 5.** Representative STEM images of Pt nanocube (a) before and (b) after potential cycling; (c) Cyclic voltammograms of Pt nanocubes (red line) and corresponding Pt(110) (blue line), Pt(100) (green line) surfaces from 0.5 M H<sub>2</sub>SO<sub>4</sub>. To enhance the resolution of the H<sub>upd</sub> peaks, CVs for the cubic NPs are recorded in sulfuric acid solution (Figure 5c), where due to concomitant adsorption/desorption of H<sub>upd</sub> and desorption/adsorption of bisulfate anions, the “H<sub>upd</sub>” peaks recorded on Pt(110) and Pt(100) are much more pronounced than in perchloric acid electrolytes.<sup>12,50</sup> HRTEM images of Pt nano-octahedron (d) before and (e) after potential cycling. (f) Cyclic voltammograms of Pt nano-octahedrons (blue line) compared with Pt polycrystalline nanoparticles (green line) and Pt(111) (red line) from 0.1 M HClO<sub>4</sub>. Because the butterfly feature recorded on Pt(111) can serve as an electrochemical fingerprint for a well-ordered surface with the hexagonal geometry, CV of octahedral NPs and Pt(111) will be compared in perchloric acid solution.

For octahedral NPs, while the HRTEM in Figure 6d shows hexagonal shape, close inspection of TEM of lower magnification unambiguously reveals that a portion of supported NPs deviate from octahedral shape (some taking on an icosahedral shape<sup>51,52</sup>) (Fig. S6c), signaling that adsorption of H<sub>upd</sub> and OH<sub>ad</sub> will deviate significantly from a CV recorded for the Pt(111) in perchloric acid solution. Indeed, a CV of octahedral NPs shows the presence of a pronounced (110)-like peak at 0.15 V and a broad H<sub>upd</sub> peak at more positive potentials (Fig. 5f). As stated above for cubo-octahedral and cubic NPs, it can be concluded that an average distribution of Pt atoms within the octahedral NPs is rather irregular, i.e., they are more Pt-poly-like than Pt(111)-like. This is expected as even well prepared Pt single crystals contain a moderate amount of surface defects. Therefore it is even less feasible to have perfect faceted NPs. Taken together, results in Figure 5 reveal that both cubic and octahedral NPs are decorated with many defects which, as we learned from single crystals, play an inherently synergistic role in controlling the potential-dependent stability and reactivity of surface atoms.

As for cubo-octahedral NPs previously, potential-dependent stability of cubic and octahedral NPs was probed after applying 4000 potential cycles to 1.1 V. By analyzing high resolution TEM images in Figure 5 as well as TEM in Figure S6 it is obvious that after the potential cycling

both the as-prepared cubic and octahedral NPs are converted to the round-like polyhedral shape. This suggests that under irreversible oxide formation/reduction cycles it is very difficult to preserve the particle shapes. Clearly, then, if the shape is lost at potentials relevant for proton exchange membrane fuel cell (PEMFC) cathodes than it would be difficult (impossible) to correlate any activity differences to the initial NP shape. Indeed, we found that cubic, octahedral and cubo-octahedral NPs with similar particle size (ca. 7-8 nm) have almost the same activity for the ORR; e.g., at 0.9 V  $\sim 1$  mA/cm<sup>2</sup> and  $\sim 350$  mA/mg<sub>Pt</sub>. We notice, the same is true if the potential is cycled to 1 V, the only difference being that the observed transformation requires more potential cycles. The potential-dependent shape transformation of Pt NPs can be considered to be guided by both thermodynamics (the driving force for an irreversible oxide formation) as well as kinetics (the rate of oxide formation which is, at the same electrode potential, mainly controlled by the density of surface defects). At this point it is also appropriate to mention that although it has been suggested that reactivity and selectivity of metal catalysts for the ORR can be tailored by controlling NP shape, our results show that this would be extremely difficult for long-term catalytic performance as the NPs will eventually be exposed to electrode potentials at which an irreversible oxide would slowly, but persistently, transform any shape-controlled activity to activity that is determined by thermodynamically stable round-like NPs.<sup>53</sup>

In summary, by comparing morphological, adsorption and catalytic properties of Pt single crystals to those of Pt NPs before and after the ORR we conclude that without understanding relationships between activity and stability of Pt single crystal surfaces it would be impossible to resolve complexities associated with the ORR on Pt NPs. We show that in establishing the particle size effect, one must take into consideration at least three important factors: (i) NPs must be uniform in size; (ii) dispersion of NPs on conductive support must be uniform; (iii) electrochemical experimental conditions used to “pre-condition” NPs for establishing the ECSA and the specific activity must follow the same protocol. With these stipulations in mind, we have shown that there is indeed a particle size effect with specific activity increasing with increasing NP diameter. However, the particle size effect begins to lose its clarity as catalyst age, especially at the smaller particles sizes, where Pt dissolution initiated by the formation of irreversible surface oxides results in dissolution/redeposition and a broadening of the particle size distribution. These same stability issues are evident when exploring the particle shape effect, e.g., structural evolution under moderate reaction conditions yielded particles of a round geometry, indiscriminate to the initial particle shape. Monodisperse 7 nm cubo-octahedral Pt NPs would be recommended as a tradeoff between initial mass activity and durability performance. We conclude that while there may in fact be a shape effect for the ORR electrocatalysis on the Pt NP, the main challenge should be placed on how to stabilize particular shape that could be associated with certain architecture of nanoparticles.<sup>54-56</sup>

## Experimental Methods

The Pt based NPs of varied sizes were synthesized using solvo-thermo method adopted from previous publications with modifications. The detailed synthesis of 2.8 nm Pt was recorded elsewhere.<sup>57</sup> The synthesis of 7.2 nm cubo-octahedral Pt NPs started by mixing 0.08 g platinum acetylacetonate  $\langle \text{Pt}(\text{acac})_2 \rangle$ , 1.0 mL oleic acid, 5.0 mL oleylamine and 10 mL benzyl ether in a three-necked flask. The solution was stirred under Ar flow for 30 minutes and was subsequently heated to 160 °C at 10 °C/min. In the meantime, 0.2 mL iron pentacarbonyl  $\text{Fe}(\text{CO})_5$  was

dissolved in 4 mL chloroform ( $\text{CHCl}_3$ ) to make 5%  $\text{Fe}(\text{CO})_5$  solution. 0.5 mL of this  $\text{Fe}(\text{CO})_5$  solution was injected to the flask at  $160^\circ\text{C}$ . The temperature was then raised to  $210^\circ\text{C}$  at  $15^\circ\text{C}/\text{min}$  and kept for one hour. The as-synthesized Pt NPs were precipitated out by adding ethanol with centrifugation. The washed NPs were subsequently collected and re-dispersed in hexane. Cubo-octahedral Pt NPs of 4 and 5 nm were synthesized by similar methods expect that the  $\text{Fe}(\text{CO})_5$  solution was introduced at  $170^\circ\text{C}$  and  $180^\circ\text{C}$ , respectively. The synthesis details were recorded in previous publications for Pt cubic NPs<sup>18</sup> and octahedral NPs.<sup>51,52</sup> The NPs were anchored onto carbon support (Tanaka 902.4  $\text{m}^2/\text{g}$ ) in chloroform by sonicating. The mass ratio of particle versus carbon was approximately 1:1. After that, the catalyst was annealed in air at  $185^\circ\text{C}$  to clean the surface.<sup>57</sup>

Pt(111), Pt(100) and Pt(100) single crystalline electrodes (6 mm in diameter) were prepared by inductive heating for 10 minutes at about 1100 K under gentle flow of forming gas (3%  $\text{H}_2$  in Ar). These electrodes were subsequently cooled down to room temperature in the same atmosphere. The surface of the electrodes was covered by a droplet of Milli-Q water before they were transferred to the electrochemical cell in hanging meniscus mode. Detailed ex-situ STM analysis of Pt single crystal surface were recorded in previous publication.<sup>38</sup>

The electrochemical characterizations of the Pt NP catalysts were carried out in a standard three-compartment electrochemical cell using 0.1 M perchloric acid ( $\text{HClO}_4$ ) or 0.5 M sulfuric acid ( $\text{H}_2\text{SO}_4$ ) as the electrolyte. A Ag/AgCl electrode was used as the reference electrode and a Pt wire served as the counter electrode. The treated catalysts were dispersed in Milli-Q water under sonication to make  $\sim 0.5$  mg/mL catalyst ink. 20-30  $\mu\text{L}$  catalyst ink was pipetted onto the glassy carbon electrode surface ( $0.283\text{ cm}^2$  geometrical surface area) to make the working electrode. The catalyst loadings were between 15 and 19  $\mu\text{g}/\text{cm}^2$ . An autolab 302 potentiostat was used to conduct the electrochemical measurement. An initial cyclic voltammogram (CV) was recorded after cycling between 0.05V and 1.0V for 50 sweeps at 50 mV/s under argon atmosphere. The oxygen reduction reaction polarization curves were obtained at 20mV/s scan rate and 1600 rpm rotation with iR drop correction when the electrolyte was saturated with oxygen. For the CO stripping experiment, the electrolyte was purged by carbon monoxide to have the surface of Pt fully covered by CO at 0.05V. After that, the electrolyte was purged by argon to remove CO. The electrode was cycled between 0.05V and 1.07V at 50mV/s for four scans. The electrochemically active surface area (ECSA) of the catalyst was calculated from CO stripping peak area. The reference electrode was calibrated by hydrogen oxidation/evolution reaction at the end of each measurement. All electric potentials shown in this paper are versus reversible hydrogen electrode (RHE). All above mentioned electrochemical measurements were conducted at room temperature ( $20^\circ\text{C}$ ). Stability test was carried out at elevated temperature ( $60^\circ\text{C}$ ), by scanning between 0.6V and 1.1V for 4000 sweeps at 50mV/s in 0.1 M  $\text{HClO}_4$  unless otherwise specified. All the electrochemical measurements were repeated at least 3 times to confirm reproducibility.

The Inductively coupled plasma mass spectrometry (ICPMS) analysis was performed on a Perkin-Elmer/SCIEX spectrometer (model Number: ELAN DRC-II). The sample flow rate is 0.83 mL/min. Transmission electron microscopy (TEM) analysis was performed on a Philips EM 30 at 200 kV. HRTEM images were collected on a FEI Tecnai F20ST AEM (200 kV). STEM images were carried out on a JEOL 2200FS TEM/STEM (200 kV) with a CEOS aberration (probe) corrector.

**Supporting Information.** Electronic Supplementary Information (ESI) available

## AUTHOR INFORMATION

### Corresponding Author

\* nmmarkovic@anl.gov

## ACKNOWLEDGMENT

The single crystal work was supported by the U.S. Department of Energy, Basic Energy Sciences, Materials Sciences and Engineering Division. The portion of work related to nanoparticle syntheses and characterization was supported by the office Energy efficiency and Renewable Energy, Fuel Cells Technologies Program and Toyota motor Engineering & Manufacturing North America. The electron microscopy was accomplished at the Electron Microscopy Center at Argonne National Laboratory, a U.S. Department of Energy Office of Science Laboratory operated under Contract No. DE-AC02-06CH11357 by UChicago Argonne, LLC. STEM studies were accomplished at the Center for Nanophase Materials Sciences at Oak Ridge National Laboratory, which is sponsored by the Scientific User Facilities Division, Office of Basic Energy Sciences, U.S. Department of Energy.

## REFERENCES

1. J. Chen, B. Lim, E. P. Lee, and Y. Xia, *Nano Today*, 2009, **4**, 81–95.
2. B. R. Cuenya, *Thin Solid Films*, 2010, **518**, 3127–3150.
3. S. Guo, S. Zhang, and S. Sun, *Angewandte Chemie International Edition*, 2013, **52**, 8526–8544.
4. J. Wu and H. Yang, *Acc. Chem. Res.*, 2013, **46**, 1848–1857.
5. B. Hammer and J. K. Nørskov, *Advances in Catalysis*, 2000, **45**, 71–129.
6. Poltorak O. M. and Boronin V. S., *Russ. J. Phys. Ch.*, 1966, **40**, 1436.
7. K. Kinoshita, *J. Electrochem. Soc.*, 1990, **137**, 845–848.
8. M. L. Sattler and P. N. Ross, *Ultramicroscopy*, 1986, **20**, 21–28.
9. N. Markovic, H. Gasteiger, and P. N. Ross, *J. Electrochem. Soc.*, 1997, **144**, 1591–1597.
10. B. Hammer and J. K. Nørskov, *Surface Science*, 1995, **343**, 211–220.
11. S. Mukerjee, S. Srinivasan, M. P. Soriaga, and J. McBreen, *J. Electrochem. Soc.*, 1995, **142**, 1409–1422.
12. N. M. Marković, R. R. Adžić, B. D. Cahan, and E. B. Yeager, *Journal of Electroanalytical Chemistry*, 1994, **377**, 249–259.
13. H. A. Gasteiger and N. M. Marković, *Science*, 2009, **324**, 48–49.
14. N. M. Markovic, H. A. Gasteiger, and P. N. Ross, *J. Phys. Chem.*, 1995, **99**, 3411–3415.
15. L. J. Bregoli, *Electrochimica Acta*, 1978, **23**, 489–492.
16. H. A. Gasteiger, S. S. Kocha, B. Sompalli, and F. T. Wagner, *Applied Catalysis B: Environmental*, 2005, **56**, 9–35.
17. K. J. J. Mayrhofer, B. B. Blizanac, M. Arenz, V. R. Stamenkovic, P. N. Ross, and N. M. Markovic, *J. Phys. Chem. B*, 2005, **109**, 14433–14440.
18. C. Wang, H. Daimon, T. Onodera, T. Koda, and S. Sun, *Angewandte Chemie*, 2008, **120**, 3644–3647.
19. M. Shao, A. Peles, and K. Shoemaker, *Nano Lett.*, 2011, **11**, 3714–3719.
20. M. Watanabe, H. Sei, and P. Stonehart, *Journal of Electroanalytical Chemistry and Interfacial Electrochemistry*, 1989, **261**, 375–387.
21. M. Nesselberger, S. Ashton, J. C. Meier, I. Katsounaros, K. J. J. Mayrhofer, and M. Arenz, *J. Am. Chem. Soc.*, 2011, **133**, 17428–17433.
22. W. Sheng, S. Chen, E. Vescovo, and Y. Shao-Horn, *J. Electrochem. Soc.*, 2012, **159**, B96–B103.
23. N. Tian, Z.-Y. Zhou, S.-G. Sun, Y. Ding, and Z. L. Wang, *Science*, 2007, **316**, 732–735.

24. T. Yu, D. Y. Kim, H. Zhang, and Y. Xia, *Angewandte Chemie International Edition*, 2011, **50**, 2773–2777.
25. N. M. Marković and P. N. Ross Jr., *Surface Science Reports*, 2002, **45**, 117–229.
26. J. Clavilier, *Journal of Electroanalytical Chemistry and Interfacial Electrochemistry*, 1979, **107**, 211–216.
27. K. Kinoshita, J. T. Lundquist, and P. Stonehart, *Journal of Electroanalytical Chemistry and Interfacial Electrochemistry*, 1973, **48**, 157–166.
28. P. J. Ferreira, G. J. la O', Y. Shao-Horn, D. Morgan, R. Makharia, S. Kocha, and H. A. Gasteiger, *J. Electrochem. Soc.*, 2005, **152**, A2256–A2271.
29. L. Tang, B. Han, K. Persson, C. Friesen, T. He, K. Sieradzki, and G. Ceder, *J. Am. Chem. Soc.*, 2010, **132**, 596–600.
30. Z. Yang, S. Ball, D. Condit, and M. Gummalla, *J. Electrochem. Soc.*, 2011, **158**, B1439–B1445.
31. M. K. Debe, *Nature*, 2012, **486**, 43–51.
32. F. El Kadiri, R. Faure, and R. Durand, *Journal of Electroanalytical Chemistry and Interfacial Electrochemistry*, 1991, **301**, 177–188.
33. N. M. Marković, H. A. Gasteiger, and P. N. Ross, *J. Phys. Chem.*, 1996, **100**, 6715–6721.
34. A. Kuzume, E. Herrero, and J. M. Feliu, *Journal of Electroanalytical Chemistry*, 2007, **599**, 333–343.
35. A. Hitotsuyanagi, M. Nakamura, and N. Hoshi, *Electrochimica Acta*, 2012, **82**, 512–516.
36. K. Itaya, S. Sugawara, K. Sashikata, and N. Furuya, *Journal of Vacuum Science & Technology A*, 1990, **8**, 515–519.
37. L. A. Kibler, A. Cuesta, M. Kleinert, and D. M. Kolb, *Journal of Electroanalytical Chemistry*, 2000, **484**, 73–82.
38. D. S. Strmcnik, D. V. Tripkovic, D. van der Vliet, K.-C. Chang, V. Komanicky, H. You, G. Karapetrov, J. P. Greeley, V. R. Stamenkovic, and N. M. Marković, *J. Am. Chem. Soc.*, 2008, **130**, 15332–15339.
39. M. Wakisaka, S. Asizawa, H. Uchida, and M. Watanabe, *Phys. Chem. Chem. Phys.*, 2010, **12**, 4184–4190.
40. I. M. Tidswell, N. M. Marković, and P. N. Ross, *Phys. Rev. Lett.*, 1993, **71**, 1601–1604.
41. R. Subbaraman, D. Tripkovic, D. Strmcnik, K.-C. Chang, M. Uchimura, A. P. Paulikas, V. Stamenkovic, and N. M. Markovic, *Science*, 2011, **334**, 1256–1260.
42. S. Motoo and N. Furuya, *Berichte der Bunsengesellschaft für physikalische Chemie*, 1987, **91**, 457–461.
43. N. M. Marković, N. S. Marinković, and R. R. Adžić, *Journal of Electroanalytical Chemistry and Interfacial Electrochemistry*, 1988, **241**, 309–328.
44. Y. Takasu, N. Ohashi, X.-G. Zhang, Y. Murakami, H. Minagawa, S. Sato, and K. Yahikozawa, *Electrochimica Acta*, 1996, **41**, 2595–2600.
45. G. A. Tritsarlis, J. Greeley, J. Rossmeisl, and J. K. Nørskov, *Catal Lett*, 2011, **141**, 909–913.
46. F. J. Perez-Alonso, D. N. McCarthy, A. Nierhoff, P. Hernandez-Fernandez, C. Strebler, I. E. L. Stephens, J. H. Nielsen, and I. Chorkendorff, *Angew. Chem. Int. Ed.*, 2012, **51**, 4641–4643.
47. V. Komanicky, K. C. Chang, A. Menzel, N. M. Markovic, H. You, X. Wang, and D. Myers, *J. Electrochem. Soc.*, 2006, **153**, B446–B451.
48. R. Jinnouchi, E. Toyoda, T. Hatanaka, and Y. Morimoto, *J. Phys. Chem. C*, 2010, **114**, 17557–17568.
49. C. M. Sánchez-Sánchez, J. Solla-Gullón, F. J. Vidal-Iglesias, A. Aldaz, V. Montiel, and E. Herrero, *J. Am. Chem. Soc.*, 2010, **132**, 5622–5624.

50. J. Clavilier and D. Armand, *Journal of Electroanalytical Chemistry and Interfacial Electrochemistry*, 1986, **199**, 187–200.
51. Y. Kang, M. Li, Y. Cai, M. Cargnello, R. E. Diaz, T. R. Gordon, N. L. Wieder, R. R. Adzic, R. J. Gorte, E. A. Stach, and C. B. Murray, *J. Am. Chem. Soc.*, 2013, **135**, 2741–2747.
52. Y. Kang, J. B. Pyo, X. Ye, R. E. Diaz, T. R. Gordon, E. A. Stach, and C. B. Murray, *ACS Nano*, 2013, **7**, 645–653.
53. V. Tripković, I. Cerri, T. Bligaard, and J. Rossmeisl, *Catal Lett*, 2014, **144**, 380–388.
54. J. Zhang, K. Sasaki, E. Sutter, and R. R. Adzic, *Science*, 2007, **315**, 220–222.
55. C. Wang, D. van der Vliet, K. L. More, N. J. Zaluzec, S. Peng, S. Sun, H. Daimon, G. Wang, J. Greeley, J. Pearson, A. P. Paulikas, G. Karapetrov, D. Strmcnik, N. M. Markovic, and V. R. Stamenkovic, *Nano Lett.*, 2011, **11**, 919–926.
56. C. Chen, Y. Kang, Z. Huo, Z. Zhu, W. Huang, H. L. Xin, J. D. Snyder, D. Li, J. A. Herron, M. Mavrikakis, M. Chi, K. L. More, Y. Li, N. M. Markovic, G. A. Somorjai, P. Yang, and V. R. Stamenkovic, *Science*, 2014, 1249061.
57. D. Li, C. Wang, D. Tripkovic, S. Sun, N. M. Markovic, and V. R. Stamenkovic, *ACS Catal.*, 2012, **2**, 1358–1362.